Sonochemically Synthesized Mesoporous Pyrophanite- $MnTiO_3/TiO_2$ Nanoparticles: Adsorbent for Removal of Commercial Malachite Green Dye

Syal, Abhinandan*+; Sud, Dhiraj

Department of Chemistry, Sant Longowal Institute of Engineering & Technology (SLIET), Longowal, Sangrur, 148106, Punjab, INDIA

ABSTRACT: *Malachite Green (MG) dye belongs to the triphenylmethane class and exhibits a noxious impact on the living being. Thus, it's being immensely important to remove it from the environment matrix. Herein, the sonochemical synthesized adsorbent material -pyrophanite-$MnTiO_3/TiO_2$ NanoParticles (NPs) was utilized to expel the commercial Malachite Green (MG) dye from the solution. The adsorption efficacy data indicate the maximum removal of MG (90.2%) is obtained for the NPs calcinated at 1000 °C (MT1). The optimized adsorption material (MT1) is characterized by using different techniques including XRD, FE-SEM, EDX, FT-IR, BJH, and BET. The XRD analysis indicates the formation of divergent phases viz. rutile TiO_2 and $MnTiO_3$. The FE-SEM indicates the formation of a nano-rod-like structure. The average size and percentage of void space of MT1 NPs are evaluated by using IMAGE J software. The hysteric loops obtain from BET and BJH plots reveal the existence of type H3 hysteresis indicating the MT1 NPs exhibit mesoporous structure. The surface area, pore volume, and pore size are 61.245 m^2/g, 0.139 cm^3/g, and 2.0178 nm respectively. The pH, dye concentration, and temperature of the solution are optimized for the removal of MG by using MT1 NPs. Further, the adsorption isotherms, kinetics studies, and intra-particle studies indicate that monolayered second-order diffusion occurs onto the surface of MT1 NPs. The adsorption process is endothermic, thermodynamically driven, and accompanied by an increase in entropy.*

KEYWORDS: *$MnTiO_3$; Malachite green; Adsorption kinetics; Adsorption isotherms; Thermodynamics.*

INTRODUCTION

Several commercial dyes are popular in various industries such as dyeing, paper, cotton, leather, cosmetic and food industries, etc [1-3]. These synthetic-colored effluents are usually very persistent due to their complex aromatic structure that is carcinogenic to human health and toxic to the aquatic ecosystem and imposes a detrimental impact on the environment matrix [4-8]. Malachite Green (MG) is a cationic dye extensively used for the dyeing of fibers and medicinal purposes like antiseptic, fungicide, antiparasitic, etc. However, the higher concentration of MG dye causes several health issues including, damage nerve system, brain, and liver, dyscrasia, anemia, and leucocytosis, and affects the growth and fertility rates for aquatic species [9,10]. Thus, it becomes of utmost

** To whom correspondence should be addressed.*
+ E-mail: abhinandan.syal87@gmail.com
1021-9986/2022/8/2548-2560 13/$/6.03

importance to remove the MG present in effluent before discharging into the main water stream. In the existing study, MG is designated as a reference dye to determine the adsorption capacity of the as-synthesized adsorbent.

To date, various dye removal processes from solutions involving conventional pre-treatment strategies such as coagulation [11], adsorption [12], photocatalytic degradation [13], microbial oxidation [14], and sonochemical and electrochemical methods [15] were adopted. In particular, adsorption and photocatalytic degradation techniques received widespread attention due to their supreme removal efficiency of pollutants from the environment matrix [16,17]. But photocatalytic degradation is a photochemical method that produced harmful secondary by-products that limit its application [18]. On the contrary, the adsorption technique is a physical method that does not generate toxic by-products. Moreover, adsorption is a much more effective, cost-cutting, and low-energy expenditure technique [19-23]. These points conjecture the superiority of the blanching of solution using the adsorption technique.

In literature, many adsorbent materials including micro-plastic,[24] silica, [25] oxide, [26] mixed oxides, [27] metal-organic framework,[28] titanate, [29] biosorbents, [30], etc. were reported for the removal of MG dye. Nowadays, the ongoing trend has diverted to one/two, or three-dimensional metal-titanate adsorbent nano-material due to their significant surface area, chemical inertness, cost-effectiveness, regularity, and well-defined structure [31,32]. *Swathi et al.* [33] synthesized $SrTiO_3$ by a solid-state reaction to the removal of acid blue 93 dye. *Taybeh et al.* [34] removed congo-red by using solid-state reaction synthesized $ZnTiO_3$ nanomaterial. However, metal titanate synthesized from solid-state reaction exhibits limitations like irregular composite distribution and non-uniform morphology. [35] *Didwal et al.* synthesized $MnTiO_3$ using the hydrothermal method and utilized it as a photocatalyst for the mineralization of various cationic dyes. [36] To our best knowledge, the area of $MnTiO_3$ as an adsorbent material to eliminate the cationic Malachite green dye from the solution remains untouched. The characteristic chemistry of Mn, enhance the tendency to capture the -OH and H_2O molecules in the aqueous phase enhances the adsorption ability. [37] Nevertheless, $MnTiO_3$ exhibits considerable stability, and biocompatibility, and is environment friendly [38,39]. These characteristics depict the significant potential of $MnTiO_3$ nanoparticles as a promising adsorbent material.

Up to now, the field of adsorption application of $MnTiO_3$ nanoparticles remains uncharted. Herein, pyrophanite-$MnTiO_3$ (MTO) is an adsorbent material. Sonochemical synthesis of nanoparticles inculcates the qualities like regularity in size, large surface area, pare down the reaction time, increase the percentage purity, etc. [40] Thus, in the present work adsorbent material is synthesized by using the sonochemical assistant solid-state reaction technique. The phase transformation and morphological study of as-synthesized nanoparticles were carried over a wide range of calcination temperatures from 550 to 1200 °C. Various adsorption parameters such as calcinate temperature of MTO, temperature, pH, and concentration of the MG dye solution were optimized. Further, different adsorption models and kinetic and thermodynamic studies are also examined.

EXPERIMENTAL SECTION

Chemicals

$Mn(CH_3COO)_2.2H_2O$, titanium (IV) n-butoxide, and Malachite green chloride ($C_{23}H_{25}ClN_2$) were bought from Sigma-Aldrich. Nitric acid, ammonia solution, and ethanol used were of the analytical grade.

Synthesis of nanoparticles

Titanium (IV) n-butoxide and manganese (II) acetate dihydrate were used as precursors of titanium and manganese respectively. 50 mL ethanol and 3.4 g of titanium (IV) n-butoxide were mixed along with magnetic stirring for 2 hours to get a homogeneous solution (solution A). 5.19 g of manganese (II) acetate dihydrate was dissolved in 50 mL of millipore water (solution B). The solutions (A and B) were mixed on a magnetic stirrer for two hours. After that, NH_4OH was added dropwise at the rate of 1mL/min along with stirring. The gelatinous precipitates formed were placed in the ultra-sonication bath (40 kHz) for 40 min. The impurities present in the resultant precipitate were removed by washing it five times with millipore water. The filtrate was dried in an oven at 100 °C for two hours. The composite was calcinated at a temperature varied from 550 to 1200 °C. (MTO).

Instrumentation

The XRD pattern of MTO was obtained using an XPERT-PRO X-ray Diffractometer with graphite

monochromatic copper radiation (CuKα) with λ= 1.5406 Å. The scanning rate was at 0.5 s^{-1} in the 2θ ranging from 20° to 80°. Model-Bruker Tensor27 was used to record the FTIR spectra of the sample. The sample was prepared with dehydrated KBr having a weight ratio (1:10; sample: KBr) over the scanning range of 400-4000 cm^{-1}. FE-SEM spectra of MTO were recorded using model JMS-7610FPlus at an accelerating voltage of 15 kV. Model-NOVA 2000e USA, N_2 adsorption analyzer was used for surface area and pores size distribution (Brunauer–Emmett–Teller (BET) and BHJ (Barrett, Joyner, and Halenda studies). Before conducting the adsorption-desorption study the sample was degassed at 150 °C for 5 h. The Scherrer equation was used to evaluate the crystalline size of as-synthesized nanoparticles. [17].

$$D = \frac{0.96\,\lambda}{\beta \cos\theta} \quad (1)$$

Where β and θ are Full-Width at Half-Maximum (FWHM) and Bragg angle, respectively.

Batch adsorption studies

The adsorption experiments and isotherm studies suspension (50 mg of MTO NPs in 50 mL of MG solution) were obtained by taking UV- spectra (model-Shimadzu UV-1800) of 4mL sample at the preselected time interval. The suspension was constantly shaking in the thermostat rotator shaker (INNOVA 42) at the rate of 120 rpm kept at 30 °C. Before recording UV spectra, the suspension was centrifugated in a thermostat configuration machine (Centrifuge 5810R) @4000 rpm for 4 min. The pH meter model-Oankton ION 2700 was used to set the pH of the dye solution. At equilibrium, the mass of the MG (mg) adsorbed per gram of MTO (q_e) was evaluated using Eq. (2).

$$q_e = \frac{(C_o - C_e)}{W} V \quad (2)$$

equilibrium is represented as C_o *and* C_e, respectively. The 0.005 L of MG solution (V) and 0.05 g of MTO adsorbent (W) were taken in a stirring flask. The same quantity of MG and MTO was taken for kinetic and thermodynamic adsorption studies in the concentration range from 10 to 80 ppm and temperature range of (20 °C- 45 °C).

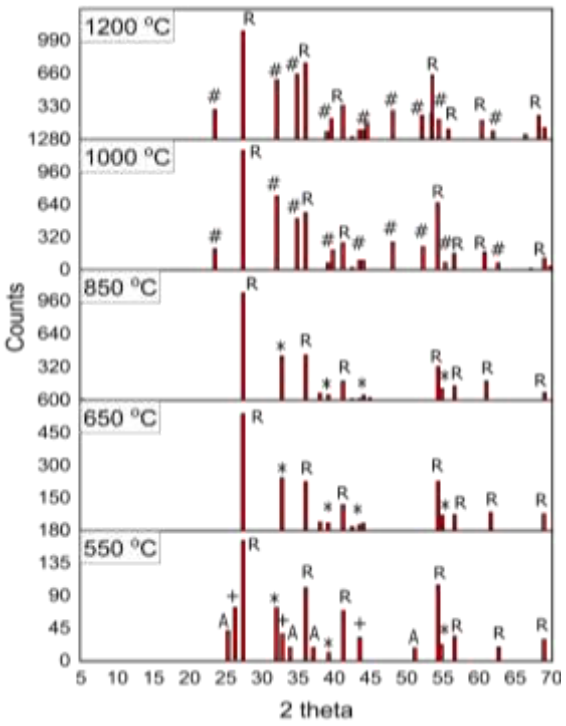

Fig. 1: XRD spectra of MTO calcinated from 550 °C to 1200 °C. [A=Anatase; R=Rutile; + =Mn_3O_4; * =Mn_2O_3; #=$MnTiO_3$].

RESULTS AND DISCUSSION

Phase and morphological analysis of MNO NPs

The XRD patterns illustrated in Fig. 1 reveal the variation of crystalline phases of MTO for the calcination of a synthesized nanomaterial at different temperatures. We have noticed at 550 °C, manganese exists in two distinct oxides viz. Mn_2O_3 (2θ= 23.1°, 32.9°, 55.1°; JCPDS- 01-071-0635) and Mn_3O_4 (2θ= 28.8°, 50.7°, 59.8°; JCPDS- 00-024-0734). TiO_2 also appeared as rutile (2θ= 27.4°, 36.0°, 41.2°, 54.3°; JCPDS- 00-02-1276) and anatase phase (2θ= 25.2°, 37.8°, 48.0°, 55.0°; JCPDS- 00-021-1272). The results obtained were as per our previous report [58]. Above 550 °C, Mn_3O_4 oxidized to Mn_2O_3 (Eq. (3)) and thermodynamically less stable anatase TiO_2 transformed to a more stable rutile TiO_2 phase. Thus, rutile TiO_2 and Mn_2O_3 phases prominent at 650 and 850 °C. At 1000 and 1200 °C, the peaks appeared at 2θ= 53.4^0 , 61.2^0 and 68.2^0 and 2θ= 27.4°, 36.0°, 41.2°, 54.3° (JCPDS 01-089-0552) corresponding to $MnTiO_3$ and TiO_2 rutile phases, respectively. The $MnTiO_3$ is formed as the result of a solid solution reaction between Mn_2O_3 and TiO_2. (Eq. (4)) The particle size of $MnTiO_3$ nanoparticles was evaluated

using the Scherrer equation (Eq. (1)) was 279 nm and 390 nm at 1000 and 1200 °C, respectively. The agglomeration of nanoparticles at 1200 °C resulted from the gain in the size at 1200 °C. From XRD investigations, it is concluded that the synthesized MTO undergoes a phase transformation at 550, 850, and 1000 °C. Further, an attempt has been made to investigate the morphological changes with phase transformation at respective temperatures and, the FE-SEM analysis was performed.

$$2Mn_3O_4 + O_2 \rightarrow 3Mn_2O_3 \quad (3)$$

$$Mn_2O_3 + 2TiO_2 \rightarrow 2MnTiO_3 + 0.5O_2 \quad (4)$$

The FE-SEM images of MNO calcinated at 550, 850, and 1000 °C temperatures are shown in Fig. 2. At 550 °C, (Fig. 2a) non-uniform agglomerated nanoparticles were formed along with nano-rods. Fe-SEM attained 850 °C (Fig. 2b) depicts the change in morphology with the appearance of globular nanoparticles. Further, with a rise in calcination temperature, the crystallinity, and porosity of nanoparticles increased. The degree of agglomeration of nanoparticles decreases at 1000 °C (Fig. 2c) and an almost uniform pattern corresponding to $MnTiO_3$ (flattened nanorods) and TiO_2 rutile (nanospheres) were attained. Thus, clear morphological changes are observed with each phase transition of MNO NPs composite. The nanoparticles become finer and more porous at 1000 °C, which increases the surface area and would enhance the adsorption property of MNO NPs.

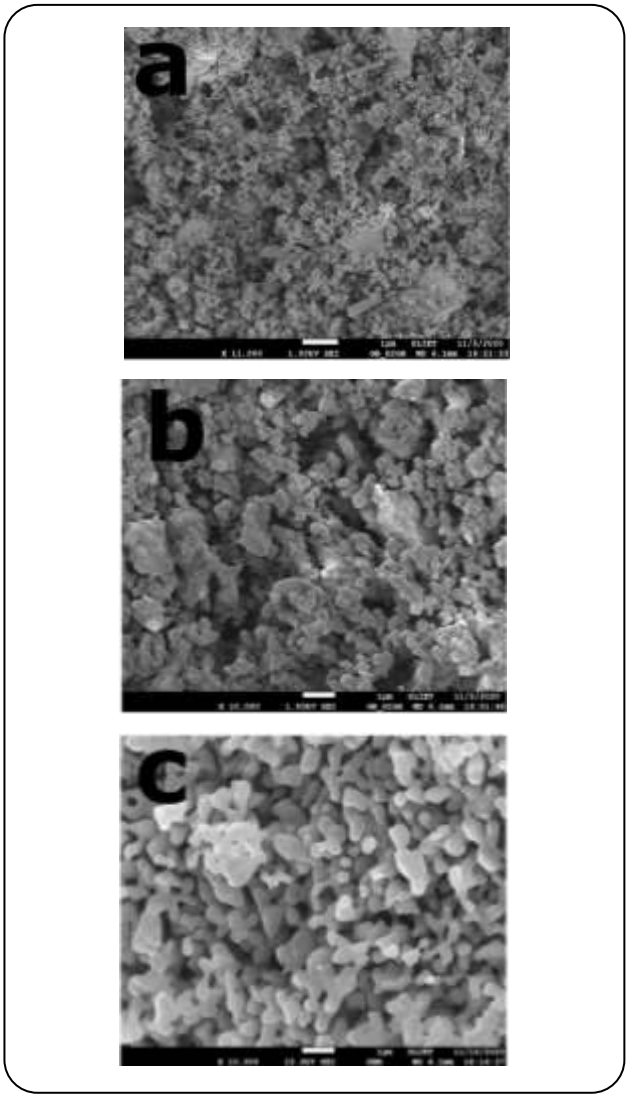

Fig. 2: FE-SEM of MTO calcinated at a) 550, b) 850 and c) 1000 °C.

Adsorption efficiency of MTO NPs

The adsorption efficiency of MTO NPs calcinated at different temperatures was investigated by using a 10 ppm aqueous solution of MG dye as a model dye. The adsorption percentage of dye onto MTO NPs calcinated at 550, 650, 850, 1000, and 1200 °C are 60.2%, 64.4%, 69%, 72% 90.2%, and 70%, respectively. (Fig. 3) The results showed the maximum removal of MG achieved by MTO NPs as an adsorbent calcinated at 1000 °C. These outcomes confirmed the adsorption ability of MTO NPs calcinated at different temperatures can be affected by particle size and phase formation. At 1000 °C, $MnTiO_3$ is formed that comprises of unique three-dimensional stacking interlayer arrangement that attributes a greater number of hydroxy groups, which enhances its adsorption ability. Thus, $MnTiO_3$ acts as a key phase for optimum

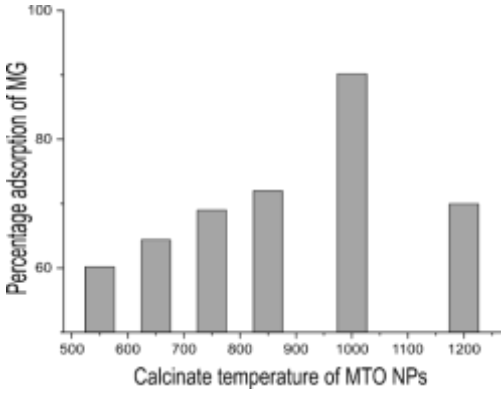

Fig. 3: Percentage adsorption of MG dye onto MTO NPs calcinated from 550 °C to 1200 °C.

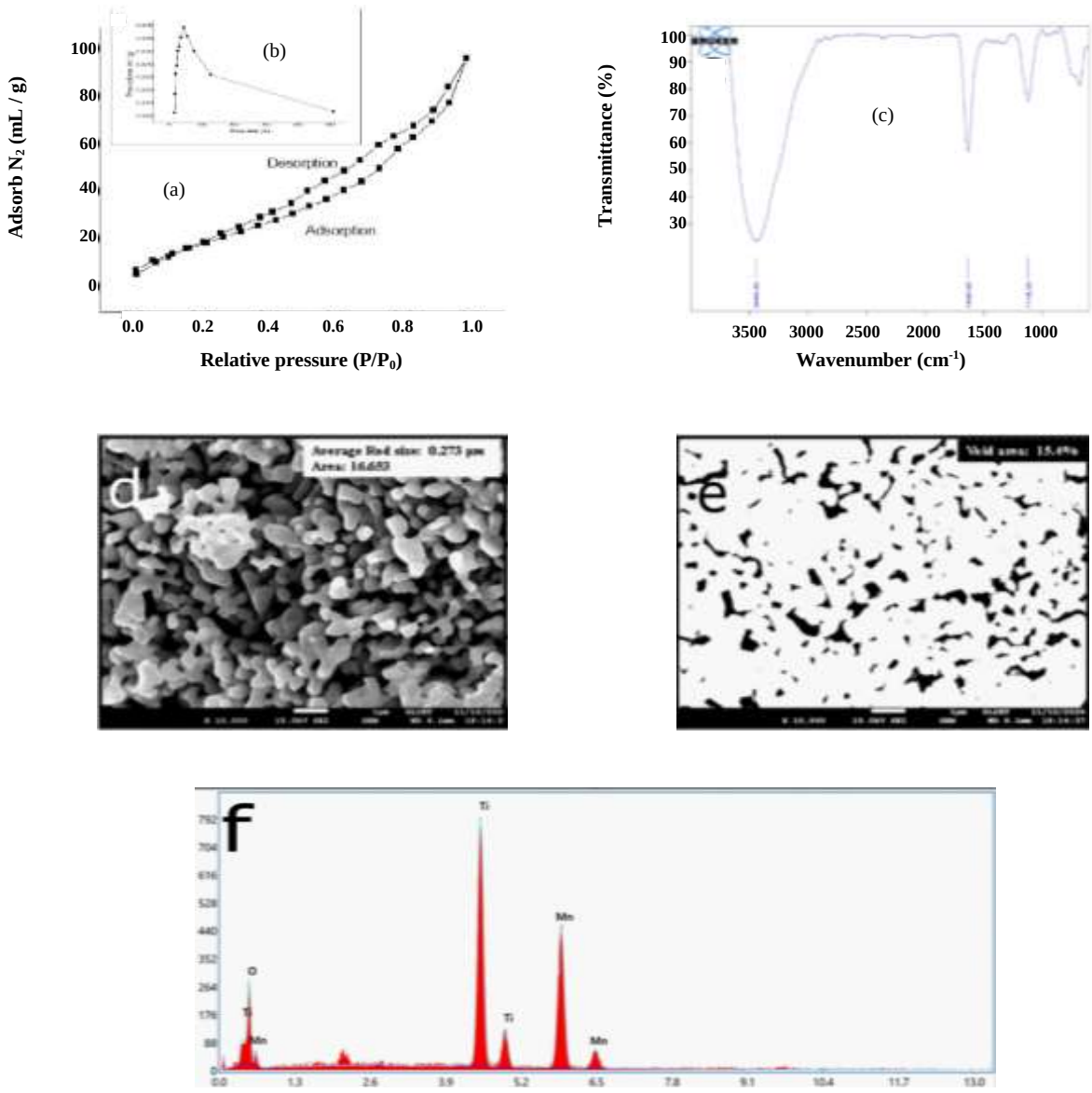

Fig. 4: Adsorption of N_2 gas onto MT1 NPs a) BET and b) BJH pore-size dispersal (inset figure). c) FTIR spectra of MT1 NPs. d) and e) FE-SEM images of MT1 NPs analyzed by Image J software to evaluate the average size and percentage of the void, respectively. f) EDX spectra of MT1 NPs

adsorption of MG. Further in-depth studies, including characterization, batch adsorption studies, and kinetic and thermodynamic studies carried out by using MTO NPs calcinated at 1000 °C. (designated as MT1)

Characterization of MT1 NPs

The surface area and nature, size, and pore volume of MT1 NPs were investigated by BET and BJH plots, respectively. The loop obtained in Fig. 4a was correlated with different types of hysteric loops as per the IUPAC system. [41] The obtained result revealed the existence of type H3 hysteresis which indicates the MT1 NPs exhibit mesoporous structure. The surface area of MT1 NPs obtained from BET analysis was 61.245 m^2/g. The BJH plot of pore volume versus pore size is shown in the inset Fig. 4b. The MT1 NPs have pore volume and pore size 0.139 cm^3/g and 2.0178 nm respectively. The pore size obtained from BJH analysis lies in the range of 2-50 nm,

and supports the mesoporous nature of MT1 NPs with regular pore size distribution as per IUPAC nomenclature. [42] Fig. 4c. depicted the FT-IR spectra of MT1 NPs. The O-H stretching vibration resulting a broad-ranging peak in spectra at 3444 cm^{-1} depicting the hydrogen-bonded H_2O molecules on the surface of MT1 NPs. The spectral peak 1632 cm^{-1} corresponds to residual O-H vibration modes of the traces of adsorbing water. The peaks that appeared in 407, 494, and 540 cm^{-1} represent the vibrational mode of Mn-O-Mn, O-Ti-O, and Mn-O bond respectively, which is in agreement with earlier reports. [43] Fig. 4d and 4e show the image analysis of FE-SEM images at 10,000 X magnification using IMAGE J software. FE-SEM image of MT1 NPs at 4300 X magnification (Fig. 4d) reflects the formation of uniform entangled structures from flattened nanorods of an average particle size of 270 nm. The obtained average size is in accordance with the size calculated using the Scherrer equation in XRD analysis. From Fig. 4E, it is observed that void spaces of 15.4%. The EDX spectra of MT1 shown in Fig. 4F indicate the MT1 NPs comprise Ti, Mn, and O elements that combine to form the respective titanate compound. The obtained result is similar to the *Enhessari et al.* report. [44].

Adsorption batch study of Malachite Green onto MT1 NPs

The MG adsorption on the MT1 NPs is the function of pH, starting concentration of MG, and the solution's temperature. The optimum pH was evaluated by varying the pH ranging from 2 to 11. Fig. 5a illustrates the percentage adsorption of MG onto MT1 NPs firstly increases up to 7 pH and then decreases. This indicates the dominance of electrostatic forces between MT1 and MG dye at neutral pH [45].

After pH, the starting concentration of dye is another criterion for the appraisal of the adsorption efficiency of the adsorbent. Fig. 5b. depicted the percentage adsorption of MG from solution onto MT1 NPs. The removal percentage of MG for 10, 20, 40, and 80 ppm solutions were found to be 90, 76, 59, and 20% respectively. The decrease in the removal efficiency with an increase in starting dye concentration is due to congestion of the active binding location of the adsorbent. In the next session, various isotherm models viz. Langmuir, Freundlich, Temkin, and Redlich-Peterson have been adopted to investigate the insets of MG adsorption onto MT1 NPs.

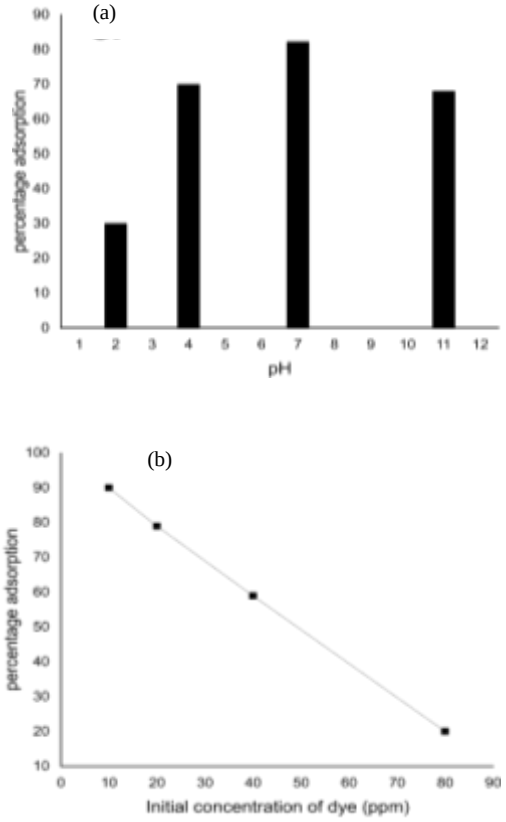

Fig. 5: a) Percentage adsorption of MG by MT1 NPs at different pH of the solution. b) Percentage adsorption of MG at preselected initial concentrations using MT1 NPs.

Equilibrium adsorption isotherm

The basis of Langmuir Isotherm (LI) is (i) homogeneous and monolayer film formation of the adsorbate on the adsorbent surface, (ii) neglecting any influence between adsorbed molecules. The Langmuir isotherm represents in Eq. (5) [46].

$$\frac{C_e}{q_e} = \frac{1}{q_m K_L} + \frac{C_e}{q_m} \quad (5)$$

Where q_m and q_e are the maximal theoretical adsorption capacity and equilibrium adsorption amount of MG in mg/g, K_L (L/mg) is the binding site of MT1 NPs, C_e is the equilibrium concentration. The best linear fitting was evaluated by plotting a graph between (C_e/q_e) and C_e. From the plot (Fig. 6a), the slope and intercept provide the values of q_m and K_L, respectively. The obtained values were summarized in Table 1.

A Freundlich isotherm model based on assumptions (i) multilayer adsorption, (ii) the adsorbed species should less

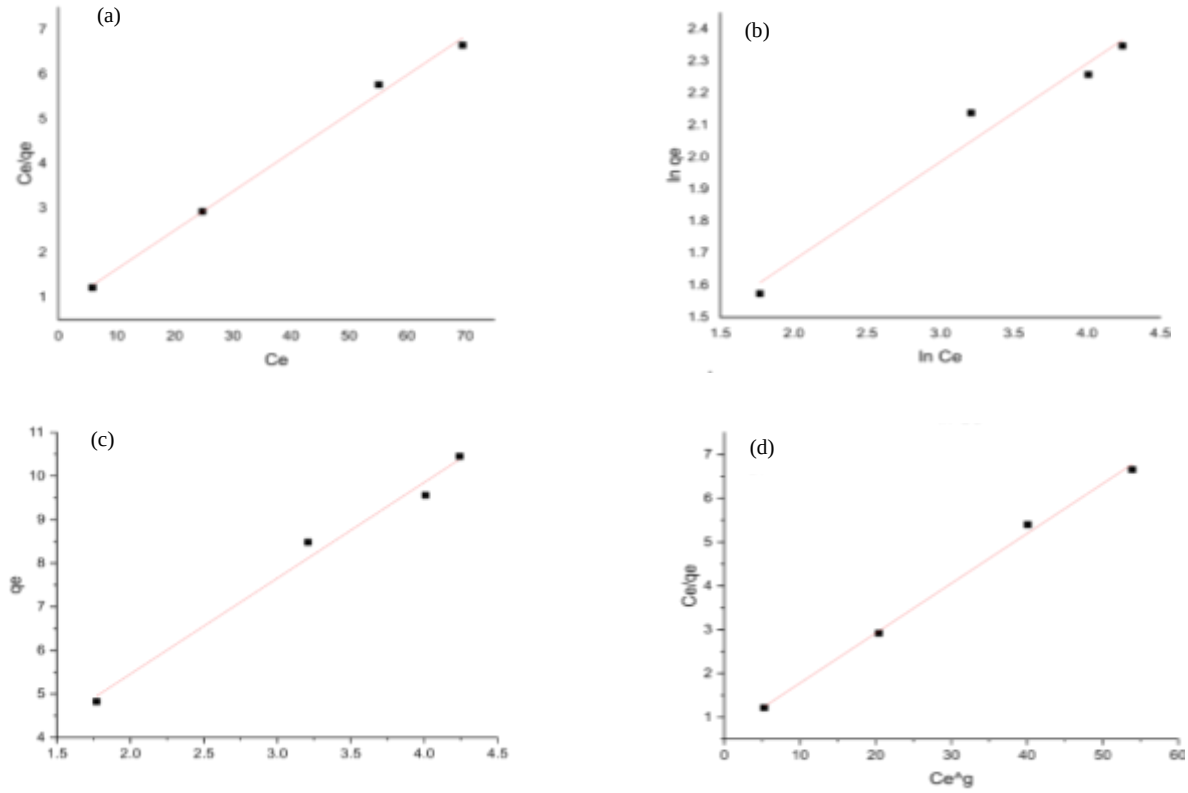

Fig. 6: Adsorption isotherms of MG dye onto MT1 NPs: a) LI, b) FI, c) Temkin, and d) Redlich-Peterson.

than or equal to the number of available active sites. Eq. (6) represents Freundlich isotherm (FI). [47]

$$\ln qe = \ln k_F + \frac{1}{n}\ln C_e \quad (6)$$

Where C_e and q_e are the same meaning as mentioned in LI. The adsorption capacity represents k_F known as the Freundlich constant (mg/g $(L/mg)^{1/n}$). From the plot in Fig. 6b, the intercept and slope provide the value of k_F and 'n' respectively and are reported in Table 1. The obtained results reveal the R^2 value for Langmuir isotherm was 0.9998 and nearby values of q_e (12.135 mg/g) with q_m (11.764 mg/g). The best fitting of isotherm where of R^2 value approach to unity and the closeness of q_m and q_e values indicates the adsorption of MG onto MT1 NPs follows the Langmuir model rather Freundlich (R^2=0.9865). The LI model suggested that mesoporous MT1 NPs contained homogenous spreading of active sites. The 'n' value greater than one, shows the adsorption conditions are feasible and the possibility of chemisorption. [48]

The chemisorption interaction of adsorbate onto the adsorbent was studied using the Temkin adsorption isotherm model. [49]

$$q_e = a + b\ln C_e \quad (7)$$

a (in g^{-1}) and *b* (J/mol) are Temkin constants representing binding constant and adsorption enthalpy respectively.

The intercept and slope of the plot between qe versus log Ce give 'a' and 'b' respectively. (Fig. 6c) The results displayed in Table 1 indicated a good correlation (R^2 =0.9971), which assured the possibility of dominant chemical forces between MG dye and MT1 nanoparticles.

Equation 8 known as Redlich-Peterson Isotherm (RPI), incorporates the characteristics of both the LI and FI. [50]

$$\frac{C_o}{q_e} = \alpha + \beta C_e^g \quad (8)$$

RPI constants 'α' and 'β' are determined from the plot between $\frac{C_o}{q_e}$ versus C_e^g. (Fig. 6d) Equation (8) transforms to LI equation when g=1 and Henry's law when g=0. The α,

Table 1: Adsorption isotherms for MG dye onto MT1 NPs at 25 ^{0}C.

Isotherm Model	Parameter	Value
Langmuir	q_e	12.135 mg/g
	q_m	11.764 mg/g
	K_L	0.1135 L/mg
	R^2	0.9998
Freundlich	K_F	2.838 $mg^{1-(1/n)}$ $L^{1/n}$ g^{-1}
	n	3.2637
	R^2	0.9865
Temkin	a	0.8735
	b	5.2783
	R^2	0.9971
Redlich- Peterson (g=0.94)	a	0.6309 mg/L
	β^g	0.1274 mg/L
	R^2	1

β, and g were evaluated from a plot between C_0/q_e and C_e^g. The value of 'g' was obtained by the hit and trial method by maximizing the R^2 value and was found to be 0.94, (Table 1) The 'g' value approaches one, which favors the occurrence of monolayer Langmuir adsorption for MG dye onto MT1 NPs.

Kinetics studies

The kinetic study of MG adsorption onto MT1 NPs was analyzed by using Lagergren's (pseudo-first-order) (FO) (Eq. (9)) [51] and Ho and McKay's equation (pseudo-second-order) (SO) (Eq. (10)) [52].

$$\log(q_{e1} - q_t) = \log q_{e1} - \left(\frac{k_1}{2.303}\right)t \quad (9)$$

$$\frac{t}{qt} = \frac{1}{(k^2 {q_{e2}}^2)} + \frac{t}{q_{e2}} \quad (10)$$

the rates constant for the FO and SO kinetics are k_1 (min^{-1}) and k_2 (g/mg min) respectively. q_t (mg/g) is the quantity of MG adsorbed at a given time (min). q_{e1} and q_{e2} denote the equilibrium amount of MG for FO and SO kinetics, respectively.

From the slopes of the plots, $\log q_{e1}$ versus t (Fig. 7a) and t/q_t versus t, (Fig. 7b) provide the values of k_1 and k_2 respectively. As compared to the plots of Fig. 7b, Fig. 7a indicated the lack of linearity as regression coefficient values were relatively poor. The obtained results were compiled in Table 2. The experimental q_{e1} and calculated q_{cal} values for the FO didn't correspond to each other and thus indicate the adsorption of MG onto MT1 NPs did not hold well for pseudo-first-order. Combinedly, a better regression coefficient ($R_2^2 =$ 0.9908-0.9976) and the closeness of q_{e2} and q_{cal} confirmed the SO kinetics for MG adsorption onto MT1 NPs accompanied by more than one step *via* chemical forces. [53]

Intra-particle diffusion (IPD) model

This model reveals the approximation concerning the mechanism behind the sorption process. *Weber et al.* [54] reported that linearity in the graph between q_t versus $t^{1/2}$ depicts the intra-particle by contrast to the inter-particle diffusion mechanism. The diffusion model is studied by using Eq. (11) [55].

$$q_t = k_{id} t^{\frac{1}{2}} + C \quad (11)$$

The poly-linear plots in Fig. 8a indicated adsorption of MG dye onto MT1 NPs follows the intra-particle diffusion mechanism. This also attributes that the adsorption mechanism comprises different steps. Nevertheless, more than one rate-determining step was controlling the adsorption of MG onto MT1 NPs. [56] From the slope and intercept of plots (Fig. 8a), the value of IPD rate constant (k_{id}) (mg/(g $min^{1/2}$)) and boundary layer constant (C)

Table 2: Kinetics parameters of FO and SO and intrapaticle-diffusion model for the adsorption of MG onto MT1 nanoparticles.

Concentration of dye (mg/l)	First order			Second order			q_{cal}	Intraparticle diffusion		
	K_1	R_1^2	q_{e1}	K_2	R_2^2	q_{e2}		K_{id}	C	R_{id}^2
10	2.1496	0.9567	4.179	0.0578	0.9908	4.826	4.131	0.822	0.704	0.9917
40	0.0548	0.8837	5.3911	0.1178	0.9927	15.698	15.21	1.2509	7.270	0.9978
80	0.0271	0.9586	3.8503	0.3355	0.9976	8.210	10.45	0.9205	4.855	0.9178

** K_1, R_1^2 and q_{e1} are the rate constant, regression coefficient, and experimental adsorption capacity respectively. K_2, R_2^2 and q_{e2} are rate constants, regression coefficient, and experimental adsorption capacity (mg/g) for the SO respectively. q_{cal} is calculated adsorption capacity (mg/g).*

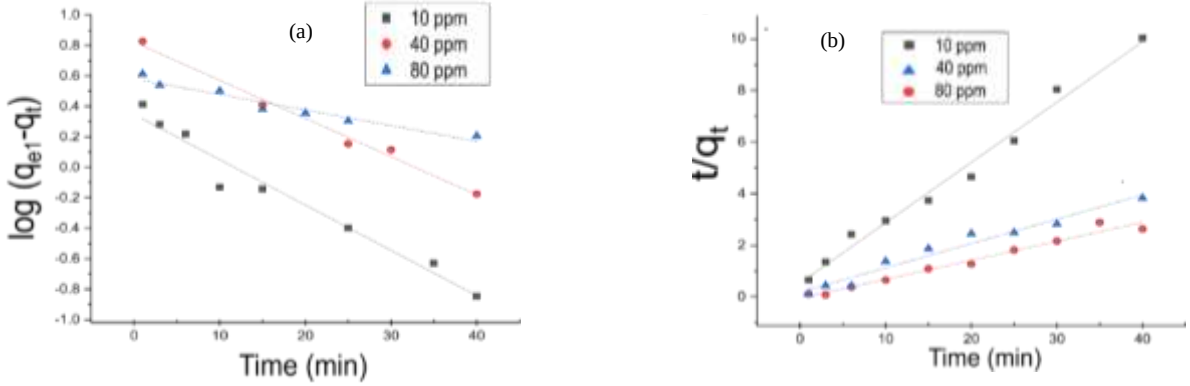

Fig. 7: Kinetics for the adsorption of 10, 40, and 80 ppm MG dye onto MT1 NPs a) FO and b) SO kinetics.

(mg/g) was obtained and summarized in Table 2**.** Data reveals that the decrease in k_{id} and 'C' value with an increase in the concentration of MG, indicates the diffusion process dominates over the boundary-layer effect [54]. The relatively poor regression coefficient obtained for 80 ppm MG solution (R^2_{id}= 0.9478) confirmed the diffusion model is best fitted for a lower concentration of MG solution (up to 40 ppm).

Thermodynamic analysis

In this session, thermodynamics analysis for the removal of MG using MT1 adsorbent is evaluated. Inset Fig. 8c, represents the adsorption of MG (10 mg/L) by MT1 NPs at the temperature ranging from 15 °C to 45 °C. The graph was plotted between q_e versus temperature. The temperature rise (15 °C to 45 °C) of the MG solution depicted the direct relation to the adsorption capacity of MG onto MT1 NPs. This adsorption behavior suggested the existence of chemical interactions between MT1 and MG dye.

Eq. (12) was used to find the ΔH°, ΔS°, and ΔG° for the removal of MG by MT1 NPs. [57]

$$\frac{\log q_e}{C_e} = \frac{\Delta S^\circ}{2.303R} - \frac{\Delta H^\circ}{2.303RT} \quad (12)$$

The intercept and slope of the graph between (q_e/C_e) verse $1/T$ provide the ΔS° and ΔH° respectively. The plot obtained in Fig. 8b displayed good linearity (R^2 =0.9909). The results were summarized in Table 3. The diffusion-controlled process showed ΔH°= +4.902 kJ/mol, revealing the endothermic nature of the adsorption of MG onto MT1 NPs. Further, the positive value of the ΔS° (+29.344 J/K.mol) indicates the adsorption of MG onto MT1 NPs proceeds along with an increase in the entropy. This increase in entropy probably releases more amount water molecules from the interface of the solid-liquid throughout the adsorption. Adsorption is feasible at high temperatures as ΔG° value became more negative. (Table 3).

Mechanism of adsorption

Herein, we proposed a plausible mechanism for the Malachite green dye adsorption onto the surface of MT1 NPs based on the results obtained in different studies. MT1 NPs comprise –Ti-Mn-O- as a stacking unit, which creates a huge number of oxygen vacancies on the surface of NPs [44].

Table 3. Thermodynamics for the adsorption of malachite green dye onto MT1 NPs.

Temperature (°C)	Initial Concentration of MG (mg/L)	ΔH° (Kj/mol)	ΔS° (j mol^{-1} K^{-1})	-ΔG° (Kj/mol)	R^2
15	20	4.902	29.344	3.549	0.9909
25				3.842	
35				4.135	
45				4.429	

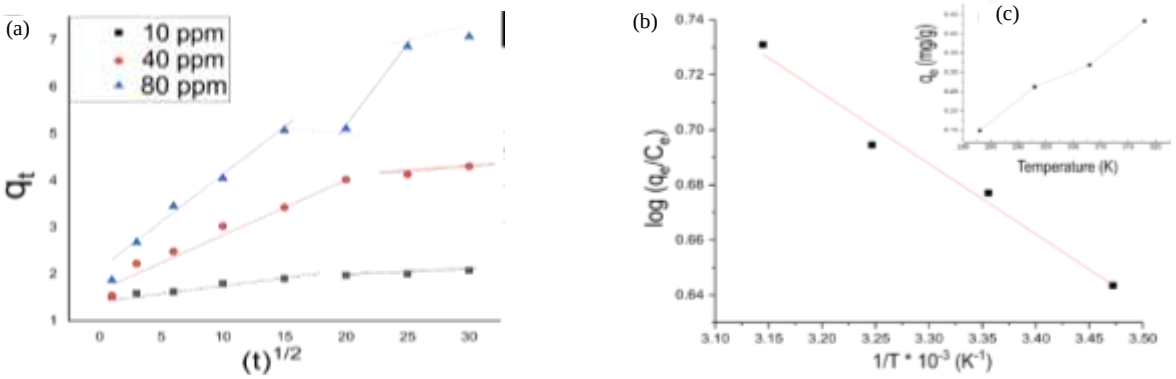

Fig. 8: Adsorption of MG dye on MT1 NPs a) Intraparticle diffusion plots, b) Graph between log (qe/Ce) versus 1/T, c) Effect of change in the temperatures on the adsorption capacity of MT1 NPs.

On these oxygen valencies, several hydroxyl groups are adsorbed (broadband observed in FT-IR at 3600 cm^{-1}). These hydroxyl groups provide the active sites for the adsorption of MG dyes to form a Langmuir monolayer. The chemical interaction is present between the hydroxyl group (negative charge oxygen) and the quaternary amine group of MG dye (positive charge). Thus, resultant adsorption is due to the electrostatic force of attraction which is as per the outcomes from pH and Temkin model study. The second-order kinetics suggests that the chemical bond is formed in two steps, the transfer of electrons through the oxygen valency. As a result, the overall energy of the system decreases with a decrease ΔG° value, indicating that the present adsorption is thermodynamically driven.

CONCLUSIONS

In summary, $MnTiO_3$ NPs were synthesized using the facile one-pot sonochemical assistant solid-state reaction technique. The synthesized NPs calcinated at 1000 °C exhibited well define nano-rod (150 nm) morphology and demonstrated the best adsorption efficiency for MG dye. BET analysis of MT1 NPs displayed mesoporous nature with average pore size and pore volume were 2.0178 nm and 0.025 cm^3/g, respectively. The reaction conditions were optimized to get the maximum performance of MT1 NPs. The maximal efficiency of the adsorbent was found at pH=7 and 10 ppm initial concentration of dye solution. Our investigation confirmed the LI fitted better than the FI suggesting the homogeneous diffusion of the active sites onto MT1 NPs with a monolayer adsorption array. Further, the RPI (R^2 =1) established these results. The results obtained from the pH and Temkin model jointly confirmed the chemical interaction exhibits between MT1 NPs and MG dye. The SO kinetic profile indicated the MG removal by MT1 associated with multi-steps accompanied by chemical forces. The SO rate constant value was 0.3355 L/mol.s. The IPD study indicated the dominating of the diffusion process over the boundary-layer effect. The adsorption thermodynamics portrayed the endothermic diffusion-control process (ΔH^0 = 4.902 kJ /mol) associated with an increase in the entropy (ΔS^0 = 29.344 J/mol·K). The negative ΔG^0 value favored the adsorption of MG onto MT1 NPs. The benefit of the mesoporous structure and strong tendency of manganese to capture OH group,

- MT1 NPs come out as promising adsorbent nano-material for the removal of cationic MG dye. Through the doping of transition metal ions in $MnTiO_3$, we supposed that the present study might be extended to synthesize a composite with a unique and more efficient adsorbent material for different dyes/heavy metal ions.

Received : Jun.. 3, 2021 ; Accepted : Sept. 20, 2021

REFERENCES

[1] Royer B., Cardoso N., Lima E., Ruiz V., Macedo T., Airoldi C., Organofunctionalized Kenyaite for Dye Removal from Aqueous Solution, *J. Colloid Interf. Sci.* **336**: 398-405 (2009).

[2] Long R. Q., Yang R.T., Carbon Nanotubes as Superior Sorbent for Dioxin Removal, *J. Am. Chem. Soc.*, **123**: 2058-2059 (2001).

[3] Amel H., Yeddou-Mezenner N., Lounis A., Eco-Friendly Scolymus Hispanicus for the Removal of Basic Blue 41, *Iran. J. Chem. Chem. Eng. (IJCCE)*, **40(2)**: 511-523 (2021).

[4] Kant R., Textile Dyeing Industry an Environmental Hazard, *J. Nat. Sci.* **4(1)**: 22-27 (2012).

[5] Mahmoodi N. M., Magnetic Ferrite Nanoparticle–Alginate Composite: Synthesis, Characterization and Binary System Dye Removal, *J. Taiwan Inst. Chem. E.*, **44(2)**: 322-330 (2013).

[6] Jaffri S.B., Ahmad K.S., Biomimetic Detoxifier *Prunus Cerasifera* Ehrh. Silver Nanoparticles: Innate Green Bullets for Morbific Pathogens and Persistent Pollutants, *Environ. Sci. Pollut. Res.*, **27**: 9669–9685 (2020).

[7] Jaffri S.B., Ahmad K.S., Phytofunctionalized Silver Nanoparticles: Green Biomaterial for Biomedical and Environmental Applications, *Rev. Inorg. Chem.*, **38(3)**: 127-149 (2018).

[8] Jaffri S.B., Ahmad K.S., Thebo Khalid H., Rehman F., Sustainability Consolidation via Employment of Biomimetic Ecomaterials with an Accentuated Photo-Catalytic Potential: Emerging Progressions, *Rev. Inorg. Chem.*, 000010151520200018 (2020).

[9] Raval N.P., Shah P.U., Shah N.K., Nanoparticles Loaded Biopolymer as Effective Adsorbent for Adsorptive Removal of Malachite Green from Aqueous Solution, *Water Conserv. Sci. Eng.*, **1**: 69-81 (2016).

[10] Radoor S., Karayil J., Jayakumar A., An Efficient Removal of Malachite Green Dye from Aqueous Environment Using ZSM-5 Zeolite/Polyvinyl Alcohol/Carboxymethyl Cellulose/Sodium Alginate Bio Composite, *J. Polym. Environ.* **29:** 2126–2139 (2021).

[11] Zhian H., Noroozi P. N., Investigating Changes in the Physical and Chemical Effects of Tartarazine Dye Remove on Industrial Wastewater by Electrocoagulation Method, *Iran. J. Chem. Chem. Eng. (IJCCE)*, **40(1)**: 123-132 (2021).

[12] Kalkan E., Nadaroglu H. Adsorptive Removal of Acid Fuchsin Dye Using By-Product Silica Fume and Laccase-Modified Silica Fume, *Iran. J. Chem. Chem. Eng. (IJCCE)*, **40(2)**: 551-564 (2021).

[13] Amini M., Ashrafi M., Photocatalytic Degradation of Some Organic Dyes Under Solar Light Irradiation Using TiO_2 and ZnO Nanoparticles, *Nano Chem. Res.* **1(1)**: 79-86 (2016).

[14] Oliveira H. S., Almeida L. D., Nb-Doped Hematite: Highly Active Catalyst for the Oxidation of Organic Dyes in Water, *Catal. Today*, **240**: 175-181 (2015).

[15] Malviya D., Sharma S., Sharma A., Verma S., Electrochemical Method for Dye Industry Waste Water Treatment, *IRJET*, **5(7)**: 2667-2673 (2018).

[16] Tan K.A., Morad N., Teng T.T., Norli I., Panneerselvam P., Removal of Cationic Dye by Magnetic Nanoparticle (Fe_3O_4) Impregnated onto Activated Maize Cob Powder and Kinetic Study of Dye Waste Adsorption, *APCBEE Procedia*, **1**: 83-89 (2012).

[17] Sud D., Syal A., Investigations on the Phase Transformation, Optical Characteristics, and Photocatalytic Activity of Synthesized Heterostructured Nanoporous Bi_2O_3–TiO_2, *J. Chin. Chem. Soc.*, **63(9)**: 776-783 (2016).

[18] Sud D., Mahajan G., Kaur M. P., Agricultural Waste Material as Potential Adsorbent for Sequestering Heavy Metal Ions from Aqueous Solutions – A Review, *Bioresour. Technol.* **99**: 6017-6027 (2008).

[19] Dbik A. Bentahar S., Messaoud, N. E., Khomr, M.E., Lacherai A., Removal of Methylene Blue from Aqueous Solution by Tunics of the Corm of the Saffron, *Iran. J. Chem. Chem. Eng. (IJCCE)*, **39(6)**: 95-104 (2020).

[20] Garg U. K., Kaur M. P., Garg V. K., Sud D., Removal of Hexavalent Chromium from Aqueous Solution by Agricultural Waste Biomass, *J Hazard Mater.*, **140(1–2)**: 60-68 (2007).

[21] Lehto J., Clearfield A., The Ion Exchange of Strontium on Sodium Titanate $Na_4Ti_9O_{20}.xH_2O$, *J. Radioanal. Nucl. Chem.*, **118(1)**: 1-13 (1987).

[22] Yang D.J., Zheng Z.F., Zhu H.Y., Liu H.W., Gao X.P., Titanate Nanofibers as Intelligent Absorbents for the Removal of Radioactive Ions from Water, *Adv. Mater.* **20(14)**: 2777-2781 (2008).

[23] Abkenar S.D., Ganjali M.R., Hossieni M., Karimi M.S., Application of Copper Vanadate Nanoparticles for Removal of Methylene Blue from Aqueous Solution: Kinetics, Equilibrium, and Thermodynamic Studies, *Iran. J. Chem. Chem. Eng. (IJCCE)*, **38(6)**: 83-92 (2019).

[24] Lin L., Tang S., Wang X., Sun X., Yu A., Hexabromocyclododecane Alters Malachite Green and Lead(II) Adsorption Behaviors onto Polystyrene Microplastics: Interaction Mechanism and Competitive Effect, *Chemosphere*, **265**: 129079 (2021).

[25] Tahir H., Atika S., Muhammad S., Synthesis of Kaolin Loaded Ag and Ni Nanocomposites and Their Applicability for the Removal of Malachite Green Oxalate Dye, *Iran. J. Chem. Chem. Eng. (IJCCE)*, **37(3)**: 11-22 (2018).

[26] Myneni V., Kanidarapu N., Vangalapati M., Methylene Blue Adsorption by Magnesium Oxide Nanoparticles Immobilized with Chitosan (CS-MgONP): Response Surface Methodology, Isotherm, Kinetics and Thermodynamic Studies, *Iran. J. Chem. Chem. Eng. (IJCCE)*, **39(6)**: 29-42 (2020).

[27] Zadvarzi S.B., Khavarpour M., Mohammad Vahdat S., Meysam Baghbanian S., Ali Shokuhi R., Synthesis of Fe_3O_4@Chitosan@ZIF-8 Towards Removal of Malachite Green from Aqueous Solution: Theoretical and Experimental Studies, *Int. J. Biol. Macromol.* **168**: 428-441 (2021).

[28] Delpiano G.R., Tocco D., Medda L., Magner E., Salis A., Adsorption of Malachite Green and Alizarin Red S Dyes Using Fe-BTC Metal Organic Framework as Adsorbent, *Int. J. Mol. Sci.*, ***22***: 788 (2021).

[29] Lesbani A., Taher T., Palapa N.R., Mohadi R., Mardiyanto M., Miksusanti M., Arsyad F.S., Removal of Malachite Green Dye using Keggin Polyoxometalate Intercalated ZnAl Layered Double Hydroxide, *Walailak J. Sci. & Tech.*, **18(10)**: 9414-9427 (2021).

[30] Dbik A., Bentahar S., El Messaoudi N., El Khomri M., Lacherai A., Removal of Methylene Blue from Aqueous Solution by Tunics of the Corm of the Saffron, *Iran. J. Chem. Chem. Eng. (IJCCE)*, **39(6)**: 95-104 (2020).

[31] Qiao X. Q., Hu F. C., Tian F. Y., Hou D. F., Li D. S., Equilibrium and Kinetic Studies on MB Adsorption by Ultrathin 2D MoS_2 Nanosheets, *RSC Adv.*, **6**: 11631-11636 (2016).

[32] Zhou M., Chen J., Zhang Y., Jiang M., Xu S., Liang Q., Li Z., Shape-Controlled Synthesis of Golf-Like, Star-Like, Urchin-Like and Flower-Like $SrTiO_3$ for Highly Efficient Photocatalytic Degradation and H_2 Production, *J. Alloys Compd.*, **817**: 152796 (2020).

[33] Gugulothu S., Singh S.A., Madras G., Superior Adsorption Capacity of Strontium Titanate and Titania Composites for Anionic Dyes Removal, *J. Environ. Chem. Eng.* **5(5)**: 4663-4675 (2017).

[34] Farahmand T., Hashemian S., Sheibani A., ZIF-Based Zinc Titanate Composite as Sufficient Sorbent for Removal Of Congo Red from Aqueous Solutions, *J. Asian Ceram. Soc.* **8(3)**: 721-732 (2020).

[35] Sharma Y. K., Kharkwal M., Uma S., Nagarajan R., Synthesis and Characterization of Titanates of the Formula $MTiO_3$ (M= Mn, Fe, Co, Ni And Cd) by Co-Precipitation of Mixed Metal Oxalates, *Polyhedron* **28**: 579–585 (2009).

[36] Didwal P. N., Mulani S. R., Patil M. S., Rupesh S. D., Photocatalytic Activity of $MnTiO_3$ Perovskite Nanodiscs for The Removal of Organic Pollutants, *Heliyon* **7**(6): e07297 (2021).

[37] Wang H., Gao Q., Li H.T., Gao M., Han B., Xia K.S., Zhou C.G., Simple and Controllable Synthesis of High-Quality $Mntio_3$ Nanodiscs and their Application as a Highly Efficient Catalyst For H_2O_2-Mediated Oxidative Degradation, *ACS Appl. Nano Mater.*, **1(6)**: 2727-2738 (2018).

[38] Ribeiro R. A. P., Andres J., Longo E., Lazaro S. R., Magnetism and Multiferroic Properties at $MnTiO_3$ Surfaces: A DFT Study, *Appl. Surf. Sci.*, **452**: 463-472 (2018).

[39] Avci C., Aydin A., Tuna Z., Yavuz Z., Yamauchi Y., Suzuki N., Dag O., Molten Salt Assisted Self Assembly (MASA): Synthesis of Mesoporous Metal Titanate ($CoTiO_3$, $MnTiO_3$, and $Li_4Ti_5O_{12}$) Thin Films and Monoliths, *Chem. Mater.*, **26(20)**: 6050-6057 (2014).

[40] Ali Dheyab, M. Aziz A.A. Jameel M.S., Recent Advances in Inorganic Nanomaterials Synthesis Using Sonochemistry: A Comprehensive Review on Iron Oxide, Gold and Iron Oxide Coated Gold Nanoparticles, *Molecules*, **26**: 2453 *(*2021).

[41] Brunauer S., Deming L.S., Deming W., Teller E., On A Theory of The Van Der Waals Adsorption of Gases, *J. Am. Chem. Soc.* **62(7)**: 1723-1732 (1940).

[42] Rouquerol J., Avnir D., Fairbridge C.W., Everett D.W., Haynes J.M., Pernicone N., Ramsay J.D.F., Sing K.S.W., Unger K.K., Recommendations for the Characterization of Porous Solids (Technical Report), *Pure Appl. Chem.*, **66(8)**: 1739-1758 (1994).

[43] Wang X., Andrews L., Infrared Spectra of $M(OH)_{1,2,3}$ (M = Mn, Fe, Co, Ni) Molecules in Solid Argon and the Character of First Row Transition Metal Hydroxide Bonding, *J. Phys. Chem. A.*, **110(33)**: 10035-10045 (2006).

[44] Enhessari M., Parviz A., Karamali E., Ozaee K., Synthesis, Characterisation and Optical Properties of $MnTiO_3$ Nanopowders, *J. Exp. Nanosci.*, **7(3)**: 327-335 (2012).

[45] Hu Y., Guo T., Ye X., Li Q., Guo M., Liu H., Wu Z., Dye Adsorption by Resins: Effect of Ionic Strength On Hydrophobic and Electrostatic Interactions, *Chem. Eng. J.*, **228**: 392-397 (2013).

[46] Langmuir I., The Constitution and Fundamental Properties of Solids and Liquids. Part I. Solids, *J. American Chem. Soc.*, **38**: 2221-2295 (1916).

[47] Arivoli S., Hema M., Martin P., Parsath D., Adsorption of Malachite Green onto Carbon Prepared from Borassus Bark, *Arab. J. Sci. Eng.*, **34(2)**: 31-42 (2009).

[48] Pan B., Xing B., Adsorption Mechanisms of Organic Chemicals on Carbon Nanotubes, *Environ. Sci. Technol.* **42(24)**: 9005-9013 (2008).

[49] Weber T. W., Chakkravorti R. K., Pore and Solid Diffusion Models for Fixed- Bed Adsorbers, *AIChE J.* **20**: 228-238 (1974).

[50] Redlich O., Peterson D. L., A Useful Adsorption Isotherm, *J. Phys. Chem.* **63(6)**:1024 (1959).

[51] Ho Y. S., McKay G., Pseudo-Second Order Model for Sorption Processes, *Process Biochem.*, **34**: 451-465 (1999).

[52] Ho Y.S., McKay G., Sorption of Dye from Aqueous Solution by Peat, *Chem. Eng. J.*, **70**: 115-124 (1998).

[53] Goscianska J., Ciesielczyk F., Lanthanum Enriched Aminosilane-Grafted Mesoporous Carbon Material for Efficient Adsorption of Tartrazine Azo Dye, *Micropor. Mesopor. Mat.*, **280***:* 7-19 (2019).

[54] Weber W. J., Morris J. C., Kinetics of Adsorption on Carbon from Solution, *J. Sanit. Eng. Div. Asce.*, **89(2)**: 31-60 (1963).

[55] Santhi T., Manonmani S., Smitha T., Kinetics and Isotherm Studies on Cationic Dyes Adsorption onto Annona Squmosa Seed Activated Carbon, *Int. J. Eng. Sci. Techno.*, **2(3)**: 287-295 (2010).

[56] Yoro K.O., Amosa M.K., Sekoai P.T., Mulopo J., Daramola M.O., Diffusion Mechanism and Effect of Mass Transfer Limitation During the Adsorption of CO_2 by Polyaspartamide in a Packed-Bed Unit, *Int. J. Sustain. Eng.* **13(1)**: 54-67 (2020),

[57] Aharoni C., Ungarish M., Kinetics of Activated Chemisorption. Part 2 -Theoretical Models, *J. Chem. Soc. Faraday Trans.*, **73**: 456-464 (1977).

[58] Sharotri N., Sud D., A Greener Approach to Synthesize Visible Light Responsive Nanoporous S-Doped TiO_2 with Enhanced Photocatalytic Activity, *New J. Chem.*, **39**: 2217-2223 (2015).